MODUMER: MODULATING TRANSFORMER FOR IMAGE RESTORATION

Anonymous authors
Paper under double-blind review

ABSTRACT

Image restoration aims to recover clean images from degraded versions. While Transformer-based approaches have achieved significant advancements in this field, they are limited by high complexity and their inability to capture omni-range dependencies, hindering their overall performance. In this work, we develop **Modumer** for effective and efficient image restoration by revisiting the *Transformer* block and *Modulation* design, which processes input through a convolutional block and projection layers, and fuses features via element-wise multiplication. Specifically, within each unit of Modumer, we integrate the cascaded Modulation design with the downsampled Transformer block to build the attention layers, enabling omni-kernel modulation and mapping inputs into high-dimensional feature spaces. Moreover, we introduce a bioinspired parameter-sharing mechanism to attention layers, which not only enhances efficiency but also improves performance. Additionally, a dual-domain feed-forward network strengthens the representational power of the model. Extensive experiments demonstrate that the proposed Modumer achieves state-of-the-art performance on **ten** different datasets for **five** image restoration tasks: image motion deblurring, image deraining, image dehazing, image desnowing, and low-light image enhancement. Furthermore, our model yields promising performance on all-in-one image restoration tasks.

1 INTRODUCTION

As a longstanding task, image restoration aims to recover a high-quality image from its degraded counterpart. It has been quite a challenging problem as infinite solutions correspond to a single input. In recent years, convolutional neural networks (CNNs) have produced promising results on this ill-posed problem by learning direct mappings from the degraded input and restored output (Qin et al., 2020; Ruan et al., 2022; Lee et al., 2021; Liu et al., 2018). However, the shortcomings of convolutional operators are obvious. Due to poor receptive field scaling (Cho et al., 2021; Chen et al., 2024), CNNs are unable to capture long-scale dependencies for powerful image representations.

Recently, Transformers have significantly advanced the state-of-the-art performance of low-level tasks (Song et al., 2022; Chen et al., 2023a; Zamir et al., 2022a). Despite having the great power to capture content-aware global perceptive fields, the self-attention (SA) layer features quadratic complexity to the input, limiting their applications in real-world scenarios. Many attempts have been made to enhance the efficiency of this expensive mechanism. SwinIR (Liang et al., 2021), Uformer (Wang et al., 2022), and Stripformer (Tsai et al., 2022) reduce the complexity of Transformer models by confining the SA operation to a fixed spatial range. Restormer (Zamir et al., 2022a) tactfully switches the operation dimension from the spatial domain to channels. Afterward, a few works explore adopting both channel SA and spatial SA in cascading or parallel manners to improve representational ability (Chen et al., 2024; Zhang et al., 2024; Chen et al., 2023c). Nonetheless, these methods impede the inherent potential of SA, originally proposed for superior global feature modeling, leading to a deterioration in restoration performance. Moreover, they mostly operate within a single scale and cannot capture multi-scale receptive fields within a single unit.

Most recently, the *Modulation* mechanism (Ma et al., 2024b), as illustrated in Figure 1 (b), considering context modeling using a large-kernel convolutional block and modulating the projected input via element-wise multiplication, has become popular in high-level vision tasks (Hou et al., 2024; Guo et al., 2023a; Yang et al., 2022). These approaches are computationally efficient and implement-

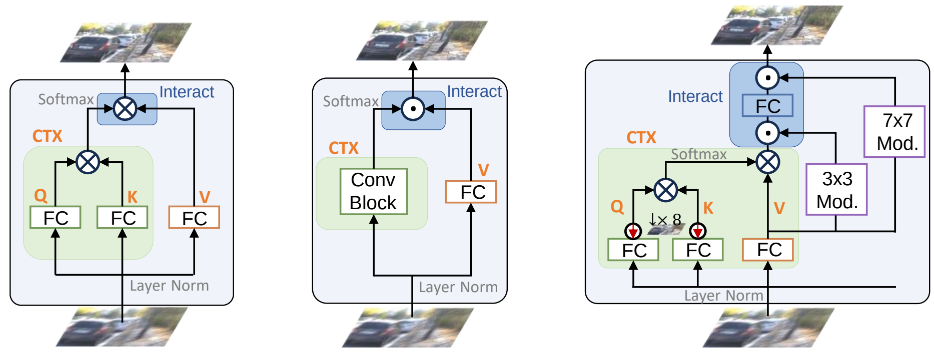

(a) Transformer block (b) Modulation design (c) Ours block

Figure 1: Comparison of Transformer block, modulation design, and our attention block. $\otimes$ and $\odot$ are matrix and element-wise multiplication, respectively. Compared to Transformer and modulation blocks, our design performs attention calculation in downsampled spaces and employs cascaded modulation operation to pursue omni-kernel feature refinement and high-dimensional representation learning. As such, the model achieves a better tradeoff between complexity and accuracy.

friendly, showing competitive performance on par with Transformer counterparts. Inspired by this modulation technique, we acquire the approximate omni-kernel feature modeling ability by integrating the Transformer layer (Figure 1 (a)) and modulation design (Figure 1 (b)) within a block. As illustrated in Figure 1 (c), the context branch (CTX) is implemented through a Transformer block at a downsampled scale, which retains the ability of SA to model global features while striking a trade-off between complexity and accuracy. The local and mesoscale receptive fields are complemented by modulating the result of SA in series using depth-wise convolutions of different kernel sizes. Compared to the canonical modulation design, our block provides real context modeling and performs cascaded modulation processes, mapping input features into higher-dimensional feature spaces. Additionally, our context branch is content-aware, which is beneficial for dealing with spatially varying degradations. Moreover, we explore a bioinspired parameter-sharing mechanism that shares parameters across different attention layers, improving both efficiency and performance.

Additionally, we present a dual-domain feed-forward network (DFFN) to improve dual-domain representation learning. Specifically, DFFN first utilizes GEGLU (Shazeer, 2020) to achieve spatial-domain signal interactions. Subsequently, the resulting features pass through the fast Fourier transform (FFT) to obtain the spectra, which are then modulated by the learnable parameters and transformed back to the spatial domain through the inverse IFFT. Next, the results interact with spatial features under the guidance of attention weights. By doing these, our DFFN achieves intra- and inter-domain interactions, improving the representational ability.

The unit of our U-shaped Modumer is built upon the above modulation-based SA block and DFFN. Unlike other Transformer-based restoration algorithms that utilize a uniform block throughout the model, we adopt a channel-wise modulation-based SA block at the initial scale to enable more efficient global feature modeling. For lower-resolution features at deeper scales, we apply spatial-wise blocks, effectively capturing spatial details. Based on these designs, Modumer achieves state-of-the-art performance on several image restoration tasks with lower complexity and fewer parameters (see Figure 2). For deraining, Modumer outperforms the previous state-of-the-art method (Zhou et al., 2024a) by 0.73 dB on AGAN-Data (Qian et al., 2018). For motion blur removal, Modumer significantly surpasses other algorithms on the HIDE dataset (Shen et al., 2019), displaying its strong capability of deblurring. Modumer also exhibits the potential on the CSD (Chen et al., 2021) dataset for the desnowing task and is superior to the previous best model (Cui et al., 2024a) by 0.74 dB in terms of PSNR. Also, on the Haze4k (Liu et al., 2021b) dataset for dehazing, it obtains 34.69 dB PSNR, an improvement of 0.54 dB over the previous state-of-the-art method (Cui et al., 2024a).

To summarize, the main contributions of this study are listed as follows:

- We present a novel attention block that consecutively modulates the self-attention results from downsampled features, providing efficient omni-kernel modulation and high-dimensional representational capability. A bioinspired parameter-sharing mechanism is introduced to improve both efficiency and performance.

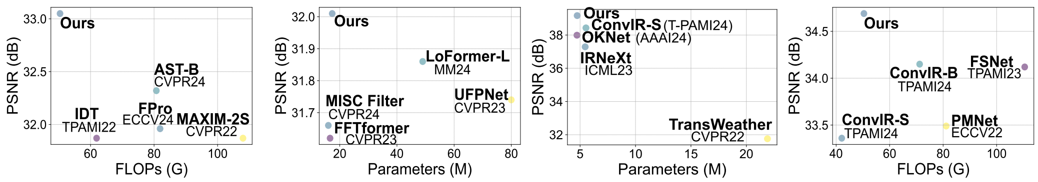

Deraining on AGAN-Data Deblurring on HIDE Desnowing on CSD Dehazing on Haze4k

Figure 2: Computation comparisons between the proposed model and state-of-the-art algorithms on AGAN-Data (Qian et al., 2018), HIDE (Shen et al., 2019), CSD Chen et al. (2021), and Haze4k (Liu et al., 2021b) for deraining, motion deblurring, desnowing, and dehazing, respectively.

- We develop a dual-domain feed-forward network that achieves spatial-spatial and spectral-spatial interactions.
- We deploy channel-wise Transformer blocks at the first scale while using spatial-wise blocks at deeper scales with lower-restoration features, resulting in our effective and efficient image restoration network, dubbed Modumer.
- Extensive experiments show that Modumer achieves state-of-the-art performance on ten benchmark datasets for five representative image restoration tasks, including image motion deblurring, image deraining, image dehazing, image desnowing, and low-light image enhancement. Moreover, Modumer produces promising performance in all-in-one scenarios.

2 Related Works

2.1 Image restoration

As a fundamental vision task, image restoration aims to reconstruct a sharp image from a degraded observation (Cho et al., 2021; Ruan et al., 2022). To resolve this heavily ill-posed problem, many conventional algorithms have been proposed based on hand-crafted features and assumptions to reduce the solution space (He et al., 2010). Recently, deep learning methods have remarkably boosted the performance of various image restoration tasks by learning generalizable features from large-scale collected data. These methods can be roughly divided into CNN-based and Transformer-based categories. CNN-based methods leverage attention mechanisms to attend to informative information for different dimensions (Qin et al., 2020; Zamir et al., 2021; Cui et al., 2023a), *e.g.,* pixel, spatial, and channel. Also, they employ advanced techniques to enlarge the receptive fields and model multi-scale features (Son et al., 2021; Liu et al., 2020; Nah et al., 2017; Jiang et al., 2020; Cui et al., 2023c), such as the encoder-decoder architecture, atrous convolution, and multi-stage learning strategy. Subsequently, Transformer methods scale the receptive field to global features via the SA layer (Tsai et al., 2022; Guo et al., 2022). To enhance its efficiency on low-level vision tasks, a few algorithms confine the SA region to fixed windows or strips (Wang et al., 2022; Liang et al., 2021; Song et al., 2022), which impedes the inherent potential of SA. Moreover, they cannot model multi-scale features within a single unit, limiting their capability for removing degradations of different sizes. In this paper, we apply SA to downsampled embedding spaces to capture global dependencies and use the cascaded modulation operation to complement the missing local information.

2.2 Modulation design

The modulation mechanism (Ma et al., 2024b; Guo et al., 2023a) considers context modeling using a large-kernel convolutional unit and modulates the projected inputs using element-wise multiplication, which has exhibited cutting-edge performance in high-level vision tasks. FocalNet (Yang et al., 2022) utilizes a stack of depth-wise convolutional layers to implement hierarchical contextualization and uses gated aggregation to selectively gather contexts. Afterward, EfficientMod (Ma et al., 2024b) adopts a simpler method for context modeling using a series of linear projections and depth-wise convolution. MambaOut (Yu & Wang, 2024) and Conv2former (Hou et al., 2024) use 7×7 depth-wise convolutions to extract contextual features. Recently, StarNet (Ma et al., 2024a) uncovers that the strong representational capacity of element-wise multiplication originates from implicitly high-dimensional spaces. However, the receptive fields of the context branch in these methods are limited. In contrast, our method involves long-range contextual signals by applying SA to downsampled embedding spaces, striking a balance between complexity and accuracy. Moreover,

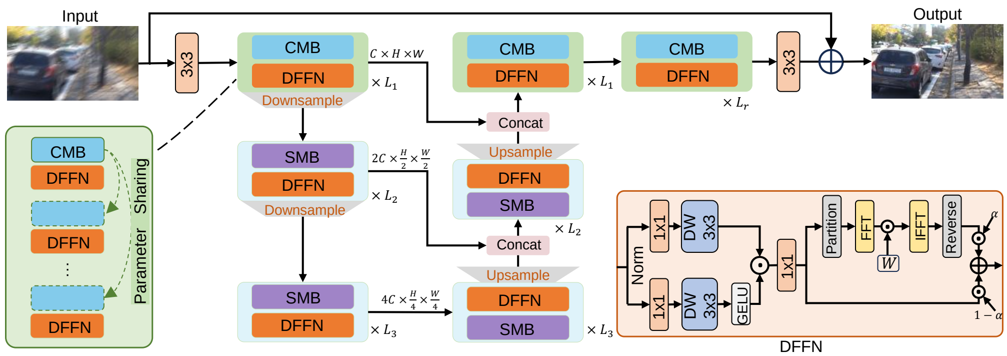

Figure 3: The network architecture of our U-shaped Modumer. We employ channel-wise modulation block (CMB) with shared parameters at the first scale while using spatial-wise modulation block (SMB) at deeper scales which involve lower-resolution features. This can strike a better balance between the complexity and the representational ability. The DFFN enhances dual-domain frequency learning via spatial-spatial and spatial-spectral interactions.

the mesoscale and local information is used to modulate the SA results via cascaded modulation, achieving omni-kernel refinement and mapping inputs into higher-dimensional spaces.

3 Methodology

In this section, we first introduce the overall architecture of Modumer. Subsequently, the proposed components are delineated individually, including two kinds of attention layers (CMB, SMB), the parameter-sharing mechanism, and the dual-domain feed-forward network (DFFN).

3.1 Overall Pipeline

Modumer follows the encoder-decoder design (see Figure 3). We employ a channel-wise modulation block (CMB) at the first scale, as the channel-wise SA can implicitly capture the large-range features efficiently while using a spatial-wise modulation block (SMB) in the other two lower-resolution scales. As such, the model strikes a better balance between complexity and representational capacity.

Specifically, given an image, we use a 3×3 convolution to extract the embedding features of size $\mathbb{R}^{C \times H \times W}$, where C denotes the channel count while $H \times W$ defines the spatial index. Subsequently, the features are fed into the three-scale encoder sub-network to produce the in-depth features. Each scale contains several Transformer blocks, whose calculation process is formulated as

$$\mathbf{X}'_k = \mathrm{CMB/SMB}(\mathbf{X}_{k-1}) + \mathbf{X}_{k-1}, \tag{1}$$
$$\mathbf{X}_k = \mathrm{DFFN}(\mathbf{X}'_k) + \mathbf{X}'_k, \tag{2}$$

where $\mathbf{X}_{k-1}$ and $\mathbf{X}_k$ are the output of the last and current Transformer block, respectively. In the encoder stage, the resolution of the features is gradually downsampled using *bilinear* interpolation while the channel capability is doubled using a 3×3 convolution. Next, the in-depth features pass through the symmetric decoder network to generate the clean features. In this process, the resolution of features is progressively restored to the original size using *bilinear* interpolation and 3×3 convolution. Meanwhile, the skip connection is adopted to combine the encoder and decoder features via concatenation. The yielded features after the three-level decoder are finally processed by a refinement stage involving r Transformer blocks and a 3×3 convolution to generate the residual image, which is added to the original input image to obtain the model output. Next, we present the internal components of the Transformer block.

3.2 Channel-wise Modulation Block (CMB)

The architectural details of CMB are illustrated in Figure 4 (a). CMB contains a downsampled channel-wise SA layer for global information modeling and two depth-wise convolutional branches modulating the SA result to complement local and mesoscale receptive fields and map features into higher-dimensional spaces. The calculation process of CMB can be formally expressed as

$$\hat{\mathbf{X}}_{\mathrm{CMB}} = W_2\left(\hat{\mathbf{X}}_{M7\times7}\left(W_1(\hat{\mathbf{X}}_{M3\times3} \odot \hat{\mathbf{X}}_{\mathrm{D-CSA}})\right)\right), \tag{3}$$

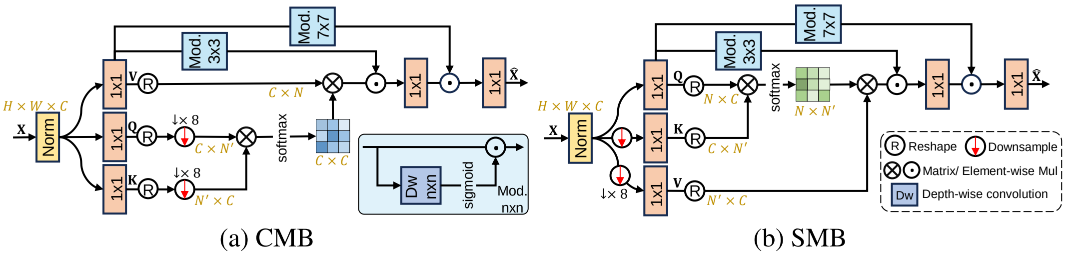

Figure 4: Module architectures of channel and spatial modulation blocks (CMB||SMB).

where $\hat{\mathbf{X}}_{\mathrm{CMB}}$, $\mathbf{X}_{\mathrm{CMB}}$ denote the output and input of CMB, respectively. D-CSA is a downsampled channel-wise self-attention layer. $\hat{\mathbf{X}}_{Mn\times n}$ is the modulation branch with the kernel size of $n \times n$, encoding local information. W_1 and W_2 are 1×1 convolutions for refinement.

D-CSA. Compared to the normal channel SA, our version computes attention maps in a downsample space, resulting in high efficiency. We assume that the number of heads is 1 and consider D-CSA as a single-head fashion. Given the normalized input $\mathbf{X}_{\mathrm{N}} \in \mathbb{R}^{C\times H\times W}$, D-CSA first utilizes the projection layers to produce query, key, and value tensors by $\mathbf{Q} = W_Q\mathbf{X}_{\mathrm{N}}$, $\mathbf{K} = W_K\mathbf{X}_{\mathrm{N}}$, and $\mathbf{V} = W_V\mathbf{X}_{\mathrm{N}}$, where $W_{(\cdot)}$ denotes parameters of 1×1 point-wise convolution. Then, the obtained $\mathbf{Q}, \mathbf{K}, \mathbf{V}$ tensors are reshaped into the size of $C \times N$, $N \times C$, and $C \times N$, respectively, where $N = H \times W$. The query and key tensors are further normalized and downsampled to prepare for cross-covariance attention. The transposed attention map is calculated by $\mathbf{Q}$ and K with size of $\mathbb{R}^{C\times C}$. The output of D-CSA can be obtained by

$$\hat{\mathbf{X}}_{\mathrm{D-CSA}} = \mathrm{Softmax}(\mathbf{QK}/\tau)\mathbf{V}, \tag{4}$$

where τ is a learnable temperature parameter and $\hat{\mathbf{X}}_{\mathrm{D-CSA}} \in \mathbb{R}^{C\times N}$ is reshaped to the original input feature size of $\mathbb{R}^{H\times W\times C}$ for further modulation operation.

Modulation design. D-CSA encodes downsampled global information while ignoring the fine-grained local details when downsampling features. To complement local information, we first filter the initially generated $\mathbf{V}$ tensor using a 3×3 depth-wise convolution, as $\mathbf{V}$ has been refined by the convolutional layer. This process is expressed as

$$\hat{\mathbf{X}}_{M3\times 3} = \mathrm{Sigmoid}(Dw_{3\times 3}(\mathbf{V})) \odot \mathbf{V}, \tag{5}$$

where $Dw_{3\times 3}$ is a depth-wise convolution of kernel size 3×3. Next, we modulate the output of D-CSA with the locally filtered result via element-wise multiplication. By doing this, the model can capture downsampled global and local dependencies and map inputs into high-dimensional spaces to improve the representational capability. To simplify the analyses, assuming the scenario involves a single-pixel input $x \in \mathbb{R}^{d\times 1}$ and a single-element output, $\hat{x} \in \mathbb{R}^{1\times 1}$, where d is the channel count, we define w_1, $w_2 \in \mathbb{R}^{1\times d}$ as convolution parameters. The modulation process involving a single convolution within each branch can be written as

$$w_1^\top x \odot w_2^\top x = \left(\sum_{i=1}^{d} w_1^i x^i\right) \odot \left(\sum_{j=1}^{d} w_2^j x^j\right) \tag{6}$$

$$= \sum_{i=1}^{d}\sum_{j=1}^{d} w_1^i w_2^j x^i x^j \tag{7}$$

$$= \underbrace{\alpha_{1,1}x^1x^1 + \cdots + \alpha_{2,3}x^2x^3 + \cdots + \alpha_{d,d}x^dx^d}_{d(d+1)/2}, \quad \alpha_{i,j} = \begin{cases} w_1^i w_2^j, & i = j, \\ w_1^i w_2^j + w_1^j w_2^i & i \neq j. \end{cases} \tag{8}$$

where i, j index the channel. We can observe that each item in Eq. 8 presents a non-linear association with x and is an individual dimension, indicating that this case achieves a representation in a $d(d+1)/2$ implicit dimensional feature space. Note that besides convolutions, the branches in our modulation design experience complicated SA, further improving the representational capability.

Additionally, we apply a 7×7 kernel branch to further modulate the preceding outcome and supply mesoscale receptive fields.

Parameter sharing. Inspired by the relationship between the hippocampus and cortex in the brain (Whittington et al., 2020; 2021), where different regions and layers of the cortex, despite performing different tasks, all receive and send information from a single shared memory in the hippocampus, we consider the attention layer as the hippocampus while the feed-forward layer as the cortex, forming our parameter-sharing mechanism illustrated in the left part of Figure 3. Interestingly, this design not only saves parameters but also improves the performance. More discussions are provided in the Appendix.

3.3 SPATIAL-WISE MODULATION BLOCK (SMB)

Figure 4 (b) presents the details of SMB, which mainly has three branches: a downsampled spatial-wise attention unit (D-SSA), and two modulation operators. The output of SMB is obtained by

$$\hat{\mathbf{X}}_{\mathrm{SMB}} = W_4 \left(\hat{\mathbf{X}}_{M7\times7} \left(W_3(\hat{\mathbf{X}}_{M3\times3} \odot \hat{\mathbf{X}}_{\mathrm{D-SSA}}) \right) \right), \tag{9}$$

where $\hat{\mathbf{X}}_{\mathrm{D-SSA}}$ is the outcome of D-SSA.

D-SSA. D-SSA is used in low-resolution scales to model spatial global features. Similarly, we also assume the number of heads is 1 to transfer D-SSA to single-head mode. Given any input $\mathbf{X} \in \mathbb{R}^{H\times W\times C}$, it is first processed by the layer normalization to yield $\mathbf{X}_{\mathrm{N}}$. Then, query ($\mathbf{Q}$), key ($\mathbf{K}$), and value ($\mathbf{V}$) tensors are produced by $\mathbf{Q} = W^Q\mathbf{X}_{\mathrm{N}}$, $\mathbf{K} = W^K\mathbf{X}_{\mathrm{N}} \downarrow$, and $\mathbf{V} = W^V\mathbf{X}_{\mathrm{N}} \downarrow$, where $\mathbf{K}$ and $\mathbf{V}$ are generated from the downsampled input ($\mathbf{X}_{\mathrm{N}} \downarrow$) for high efficiency. After reshaping $\mathbf{Q}$, $\mathbf{K}$, and $\mathbf{V}$ to new tensors of size $N \times C$, $C \times N'$, $N' \times C$, respectively, where $N = H \times W$ and $N' = H/8 \times W/8$, the calculation process of D-SSA is formulated as

$$\hat{\mathbf{X}}_{\mathrm{D-SSA}} = \mathrm{Softmax}(\frac{\mathbf{QK}}{\sqrt{C}})\mathbf{V}. \tag{10}$$

Modulation design. Similar to CMB, we utilize a cascaded modulation design with kernel sizes of 3×3 and 7×7 to complement local and mesoscale information. As such, the model is equipped with an approximate omni-kernel modulation ability, *i.e.,* local-mesoscale-global.

3.4 DUAL-DOMAIN FEED-FORWARD NETWORK (DFFN)

DFFN facilitates the spatial-spatial and spatial-spectral interactions for high-fidelity reconstruction. Figure 3 illustrates the architecture. To be specific, given input features $\mathbf{X} \in \mathbb{R}^{H\times W\times C}$, after the layer normalization, DFFN first performs GEGLU (Shazeer, 2020) as

$$\hat{\mathbf{X}}_{\mathrm{S-S}} = W_7 \left(\mathrm{GELU} \left(Dw_3^1 W_5(\mathbf{X}_{\mathrm{N}}) \right) \odot Dw_3^2 W_6(\mathbf{X}_{\mathrm{N}}) \right) \tag{11}$$

where W_5, W_6 and W_7 denote 1×1 convolutions. Dw_3^1 and Dw_3^2 are 3×3 depth-wise convolutions. $\mathbf{X}_{\mathrm{N}}$ is the normalized input and $\hat{\mathbf{X}}_{\mathrm{S-S}}$ is the spatial-spatial interaction output.

Furthermore, DFFN conducts spatial-spectral interactions by adding the Fourier-domain refined result and spatial features together under the guidance of learnable attention weights. The calculation process can be formulated as

$$\hat{\mathbf{X}}_{\mathrm{DFFN}} = \alpha\mathbf{X}_{\mathrm{Spectral}} + (1-\alpha)\hat{\mathbf{X}}_{\mathrm{S-S}} \tag{12}$$

$$\mathbf{X}_{\mathrm{Spectral}} = \mathcal{P}^{-1}\Big(\mathcal{F}^{-1}\Big(W \odot \big(\mathcal{F}(\mathcal{P}(\hat{\mathbf{X}}_{\mathrm{S-S}}))\big)\Big)\Big) \tag{13}$$

where $\mathcal{F}$ and $\mathcal{F}^{-1}$ denote the fast Fourier transform and the inverse transform, respectively. $\mathcal{P}$ and $\mathcal{P}^{-1}$ are windows partition operation and the inverse transformation, respectively. W is the learnable parameter to filter the frequency signals. α is the learnable parameter to control dual-domain information aggregation.

4 EXPERIMENTS

To validate the efficacy of the proposed Modumer, we evaluate the model on two kinds of tasks, general image restoration and all-in-one image restoration. The former trains different model copies for different datasets while the latter uses a single model for different degradation types and levels. In this section, we first present the implementation details, experimental results, and ablation studies for general image restoration. Subsequently, we apply our model to the all-in-one settings.

Figure 5: Visual comparisons on the raindrop AGAN-Data (Qian et al., 2018) dataset.

Table 1: The dataset summary for five tasks under general image restoration.

Task	Deraining	Motion deblurring	Dehazing	Desnowing	Low-light image enhancement
Dataset	SPAD‖AGAN-Data	GoPro‖HIDE	Haze4k‖GTA5	CSD‖SRRS‖Snow100K	LOL-v2

Table 2: Quantitative comparisons on AGAN-Data (Qian et al., 2018) for raindrop removal.

Methods	**PSNR**	**SSIM**
Uformer (Wang et al., 2022)	29.42	0.906
TransWeather (Valanarasu et al., 2022)	30.17	0.916
Quan *et al.* (Quan et al., 2019)	31.37	0.918
AttenGAN (Qian et al., 2018)	31.59	0.917
IDT (Xiao et al., 2022)	31.87	0.931
MAXIM-2S (Tu et al., 2022)	31.87	0.935
AWRCP (Ye et al., 2023)	31.93	0.931
FPro (Zhou et al., 2024b)	31.96	0.937
AST-B (Zhou et al., 2024a)	32.32	0.935
Ours-S	**33.05**	**0.946**

Table 3: Quantitative results on SPAD (Wang et al., 2019) for rain streak removal.

Methods	**PSNR**	**SSIM**
SEIDNet (Lin et al., 2022)	44.96	0.9911
Fu *et al.* (Fu et al., 2023)	45.03	0.9907
Restormer (Zamir et al., 2022a)	46.25	0.9911
SCD-Former (Guo et al., 2023b)	46.89	0.9941
IDT (Xiao et al., 2022)	47.34	0.9929
Uformer Wang et al. (2022)	47.84	0.9925
DRSformer (Chen et al., 2023b)	48.53	0.9924
FPro (Zhou et al., 2024b)	48.99	0.9936
AST-B (Zhou et al., 2024a)	49.51	**0.9942**
Ours-S	**49.57**	**0.9942**

4.1 General image restoration

4.1.1 Implementation details

We evaluate our model on five representative tasks with **ten** benchmark datasets. The used datasets are summarized in Table 1. We adopt the dual-domain loss functions (Cho et al., 2021; Kong et al., 2023; Cui et al., 2023a) to train the network for 300,000 iterations with the Adam optimizer. The deblurring task needs another 300,000 iterations following (Kong et al., 2023). The initial learning is set to $1\mathrm{e}^{-3}$, which is gradually reduced to $1\mathrm{e}^{-7}$ with the cosine annealing strategy. The patch size is set to 128×128 and the batch size is 32. We adopt the same data augmentation strategy as (Zamir et al., 2022a). The window size in DFFN and the downsampling ratio in SA are set to 8. According to the complexity of different datasets, we present two model versions, Modumer-S (small) and Modumer-B (base). For Modumer-S, we set the channel count to 42, and [L_1,L_2,L_3,L_r] as [2,2,4,4], while for the base model, we set the channel number to 48, and [6,6,13,4] for [L_1,L_2,L_3,L_r]. FLOPs are measured on $3 \times 256 \times 256$ patches. Due to the space limit, image enhancement results and more visualizations are presented in the Appendix. In tables, the best results are **highlighted**.

4.1.2 Results

Image deraining. The numerical results on the raindrop dataset AGAN-Data (Qian et al., 2018) are presented in Table 2. Our method significantly outperforms the recent Transformer-based AST-B (Zhou et al., 2024a) and FPro (Zhou et al., 2024b) by 0.73 dB and 1.09 dB, respectively, while consuming lower complexity, as illustrated in Figure 2 (a). Figure 5 shows that our method is more effective in raindrop removal than competitors. Moreover, the comparison results on the rain streak dataset SPAD (Wang et al., 2019) are reported in Table 3. As seen, our method achieves the best performance in terms of PSNR, outperforming the previous state-of-the-art algorithm (Zhou et al., 2024a) by 0.06 dB PSNR.

Image motion deblurring. We conduct experiments for motion deblurring on the GoPro (Nah et al., 2017) dataset and compare our results with state-of-the-art works in Table 4. Our method significantly surpasses the recent frequency-based Transformer model (Mao et al., 2024) by 0.18 dB PSNR while using 65% fewer parameters. Compared to the recent convolutional network ConvIR-L (Cui et al., 2024a), our method achieves a notable gain of 0.99 dB PSNR with comparable parameters and FLOPs. The visual results in Figure 6 show that our model recovers more structural details from

Table 4: Image motion deblurring results. Our model is trained only on the GoPro Nah et al. (2017) dataset and directly applied to the GoPro (Nah et al., 2017) and HIDE Shen et al. (2019) datasets.

Methods	**GoPro** PSNR	SSIM	**HIDE** PSNR	SSIM	**Params** (M)	**FLOPs** (G)
DMPHN (Zhang et al., 2019a)	31.20	0.940	29.09	0.924	-	-
DBGAN (Zhang et al., 2020)	31.10	0.942	28.94	0.915	11.6	760
Restormer (Zamir et al., 2022a)	32.92	0.961	31.22	0.942	26.1	135
Stripformer (Tsai et al., 2022)	33.08	0.962	31.03	0.940	20.0	170
GRL (Li et al., 2023)	33.93	0.968	31.65	0.947	20.2	1289
UFPNet (Fang et al., 2023)	34.06	0.968	31.74	0.947	80.3	243
FSNet (Cui et al., 2023b)	33.29	0.963	31.05	0.941	13.28	111
FFTformer (Kong et al., 2023)	34.21	**0.969**	31.62	0.946	16.6	131
ConvIR-L (Cui et al., 2024a)	33.28	0.963	-	-	14.83	129
MLWNet-B (Gao et al., 2024)	33.83	0.968	-	-	-	108
MISC Filter (Liu et al., 2024)	34.10	**0.969**	31.66	0.946	16.0	-
LoFormer-L (Mao et al., 2024)	34.09	**0.969**	31.86	**0.949**	49.0	126
Ours-B	**34.27**	**0.969**	**32.01**	**0.949**	17.35	139

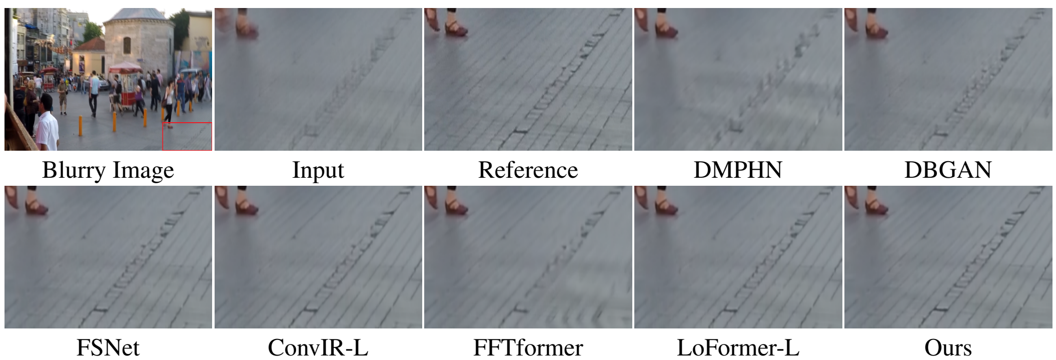

Figure 6: Deblurred results on the GoPro (Nah et al., 2017) dataset. Compared to other algorithms, the proposed method restores more details and clearer structures from the input.

Table 5: Image dehazing comparisons on the Haze4k (Liu et al., 2021b) dataset.

Methods	PSNR	SSIM
MSBDN (Dong et al., 2020a)	22.99	0.85
FFA-Net (Qin et al., 2020)	26.96	0.95
DMT-Net (Liu et al., 2021c)	28.53	0.96
PMNet (Ye et al., 2022)	33.49	0.98
FSNet (Cui et al., 2023b)	34.12	**0.99**
ConvIR-S (Cui et al., 2024a)	33.36	**0.99**
ConvIR-B (Cui et al., 2024a)	34.15	**0.99**
Ours-S	**34.69**	**0.99**

Table 6: Quantitative results on GTA5 (Yan et al., 2020) for night haze removal.

Methods	PSNR	SSIM
MRP (Zhang et al., 2017)	20.92	0.646
Ancuti *et al.* Ancuti et al. (2016)	20.59	0.623
CycleGAN (Engin et al., 2018)	21.75	0.696
Yan *et al.* (Yan et al., 2020)	27.00	0.850
Jin *et al.* Jin et al. (2023)	30.38	0.904
ConvIR-S Cui et al. (2024a)	31.68	0.917
ConvIR-B Cui et al. (2024a)	31.83	0.921
Ours-S	**32.04**	**0.928**

the hard example. We further apply our model pre-trained on GoPro to the HIDE (Shen et al., 2019) dataset. The quantitative results presented in Table 4 show that our method obtains the best result in PSNR with a prominent gain of 0.15 dB over the second-best LoFormer-L (Mao et al., 2024), demonstrating the better generalization ability of our model.

Image dehazing. We perform dehazing experiments on the Haze4k (Liu et al., 2021b) dataset. The numerical results are presented in Table 5. Our model attains a significant performance gain of 0.54 dB PSNR over the recent algorighm (Cui et al., 2024a) with lower FLOPs, as illustrated in Figure 2 (d). Compared to the CNN-based method FSNet (Cui et al., 2023b), our advantage is more obvious with much lower complexity. Figure 7 shows that our model can better deal with haze degradations than other algorithms. Additionally, we provide comparison results on a nighttime dehazing dataset GTA5 (Yan et al., 2020) in Table 6. Our Modumer-S is still superior to the strong competitors.

Figure 7: Image dehazing comparisons on the Haze4k (Liu et al., 2021b) dataset.

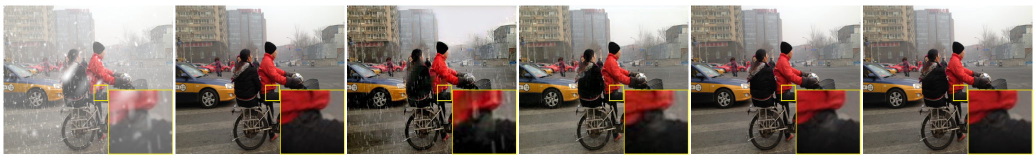

Figure 8: Image desnowing comparisons on the CSD Chen et al. (2021) dataset.

Table 7: Image desnowing comparisons on three widely-used datasets: CSD (Chen et al., 2021), SRRS (Chen et al., 2020), and Snow100K (Liu et al., 2018).

Methods	**CSD** PSNR	SSIM	**SRRS** PSNR	SSIM	**Snow100K** PSNR	SSIM	**Params** (M)	**FLOPs** (G)
DesnowNet (Liu et al., 2018)	20.13	0.81	20.38	0.84	30.50	0.94	15.6	1.7K
JSTASR (Chen et al., 2020)	27.96	0.88	25.82	0.89	23.12	0.86	65	-
HDCW-Net (Chen et al., 2021)	29.06	0.91	27.78	0.92	31.54	0.95	6.99	9.78
SMGARN (Cheng et al., 2022)	31.93	0.95	29.14	0.94	31.92	0.93	6.86	450.3
TransWeather (Valanarasu et al., 2022)	31.76	0.93	28.29	0.92	31.82	0.93	21.9	5.64
MSP-Former (Chen et al., 2023a)	33.75	0.96	30.76	0.95	33.43	**0.96**	2.83	4.42
OKNet (Cui et al., 2024b)	37.99	0.99	31.70	**0.98**	33.75	0.95	4.72	39.67
IRNeXt (Cui et al., 2023c)	37.29	**0.99**	31.91	**0.98**	33.61	0.95	5.46	42.09
ConvIR-S (Cui et al., 2024a)	38.43	**0.99**	32.25	**0.98**	33.79	0.95	5.53	42.1
Ours-S	**39.17**	**0.99**	**32.48**	**0.98**	**34.58**	**0.96**	4.74	50.39

Image desnowing. Furthermore, we verify the effectiveness of our model in snow removal using three datasets: CSD (Chen et al., 2021), SRRS Chen et al. (2020), and Snow100K Liu et al. (2018). The quantitative results are presented in Table 7. With similar computation overhead, our method achieves 39.17 dB PSNR on the CSD dataset, 0.74 dB higher than the second-best algorithm (Cui et al., 2024a). The superiority of our model can also be found on the other two datasets, demonstrating the effectiveness of our model in snow removal. Figure 8 shows that our model yields a more favorable image by removing more snow degradations.

4.1.3 Ablation studies

We perform ablation studies by training our small model for 70,000 iterations on GoPro (Nah et al., 2017). More ablation results can be found in the Appendix.

Table 8: Ablation studies for each component.

Mod. 3×3	Mod. 7×7	Sharing	DFFN	PSNR	Params.
	✓	✓	✓	31.70	4.72M
✓		✓	✓	31.69	4.64M
✓	✓		✓	31.78	4.79M
✓	✓	✓		31.69	4.74M
✓	✓	✓	✓	31.82	4.74M

Table 8 shows the results of individually removing the proposed component from the complete model. Removing our modulation branch leads to degraded performance compared to the full model. Our parameter-sharing mechanism achieves 0.04 dB PSNR performance improvement while consuming fewer parameters. Employing only the spatial-spatial interactions, *i.e.,* GEGLU, in the feed-forward network achieves 31.69 dB PSNR, which is 0.13 dB lower than our full model. These results demonstrate the effectiveness of our proposed modules and mechanism.

Input Reference AirNet PromptIR AdaIR Ours

Figure 9: Visual comparisons on the Rain100 (Yang et al., 2017) dataset under the all-in-one setting. The image produced by our model is closer to the reference image, such as the background regions.

Table 9: Dataset summary for all-in-one image restoration. Motion deblurring and low-light enhancement are only used for the five-task setting.

Task	Desnoiwing	Dehazing	Deraining	Motion deblurring	Low-light enhancement
Train	BSD400‖WED	RESIDE	Rain100L	GoPro	LOL-v1
Test	BSD68	SOTS-Outdoor	Rain100L	GoPro	LOL-v1

Table 10: Quantitative comparisons on three image restoration tasks under the all-in-one setting.

	Denoising on BSD68						**Deraining on Rain100L**		**Dehazing on SOTS**		**Average**	
	$\sigma = 15$		$\sigma = 25$		$\sigma = 50$							
Method	PSNR	SSIM	PSNR	SSIM	PSNR	SSIM	PSNR	SSIM	PSNR	SSIM	PSNR	SSIM
BRDNet (Tian et al., 2020)	32.26	0.898	29.76	0.836	26.34	0.693	27.42	0.895	23.23	0.895	27.80	0.843
LPNet (Gao et al., 2019)	26.47	0.778	24.77	0.748	21.26	0.552	24.88	0.784	20.84	0.828	23.64	0.738
FDGAN (Dong et al., 2020b)	30.25	0.910	28.81	0.868	26.43	0.776	29.89	0.933	24.71	0.929	28.02	0.883
MPRNet (Zamir et al., 2021)	33.54	0.927	30.89	0.880	27.56	0.779	33.57	0.954	25.28	0.955	30.17	0.899
DL (Fan et al., 2019)	33.05	0.914	30.41	0.861	26.90	0.740	32.62	0.931	26.92	0.931	29.98	0.876
AirNet (Li et al., 2022)	33.92	0.933	31.26	0.888	28.00	0.797	34.90	0.968	27.94	0.962	31.20	0.910
PromptIR (Potlapalli et al., 2023)	33.98	0.933	31.31	0.888	28.06	0.799	36.37	0.972	30.58	0.974	32.06	0.913
AdaIR (Cui et al., 2024c)	34.12	0.935	31.45	0.892	28.19	0.802	38.64	0.983	31.06	**0.980**	32.69	0.918
Ours	**34.15**	**0.936**	**31.50**	**0.893**	**28.25**	**0.805**	**38.78**	**0.984**	**31.17**	0.979	**32.77**	**0.919**

4.2 All-in-one image restoration

4.2.1 Implementation details

Following the recent algorithm (Potlapalli et al., 2023; Cui et al., 2024c), we perform all-in-one experiments under three-task and five-task settings with Modumer-B. The dataset summary is presented in Table 9. The model is trained on 32 samples of size 128×128 in an iteration with a learning rate of $2e^{-4}$ using Adam. The models are trained for 150 epochs with L_1 loss function.

4.2.2 Results

For the three-task setting, the model is trained on the mixed datasets obtained from denoising, dehazing, and deraining. Table 10 shows that our model achieves an average score of 32.77 dB PSNR, 0.08 dB higher than the recent frequency-based AdaIR (Cui et al., 2024c). Moreover, our method attains the best performance on most metrics. Particularly on the deraining problem, a 0.14 dB performance gain is produced by our model over AdaIR. Figure 9 demonstrates that our model is more effective in removing rain streaks, resulting in a noticeably cleaner image. We provide the result for the five-task scenario in the Appendix.

5 Conclusion

This study presents an effective and efficient Transformer model for image restoration, termed Modumer. The model incorporates the different downsampled self-attention layers with cascaded modulation designs, which can model omni-receptive field features, obtain a better balance between complexity and accuracy, and map features into high-dimensional spaces. Moreover, we investigate a bioinspired parameter-sharing mechanism in attention layers, improving efficiency and performance. In addition, we introduce a feed-forward network to facilitate intra- and inter-domain interactions. Extensive experimental results on ten datasets for general image restoration and two all-in-one settings demonstrate the effectiveness of our model.

REFERENCES

Cosmin Ancuti, Codruta O Ancuti, Christophe De Vleeschouwer, and Alan C Bovik. Night-time dehazing by fusion. In *IEEE International Conference on Image Processing*, pp. 2256–2260, 2016.

Yuanhao Cai, Hao Bian, Jing Lin, Haoqian Wang, Radu Timofte, and Yulun Zhang. Retinexformer: One-stage retinex-based transformer for low-light image enhancement. In *Proceedings of the IEEE International Conference on Computer Vision*, 2023.

Liangyu Chen, Xiaojie Chu, Xiangyu Zhang, and Jian Sun. Simple baselines for image restoration. In *Proceedings of the European Conference on Computer Vision*, 2022.

Sixiang Chen, Tian Ye, Yun Liu, Taodong Liao, Jingxia Jiang, Erkang Chen, and Peng Chen. Msp-former: Multi-scale projection transformer for single image desnowing. In *IEEE International Conference on Acoustics, Speech and Signal Processing*, pp. 1–5, 2023a.

Wei-Ting Chen, Hao-Yu Fang, Jian-Jiun Ding, Cheng-Che Tsai, and Sy-Yen Kuo. Jstasr: Joint size and transparency-aware snow removal algorithm based on modified partial convolution and veiling effect removal. In *Proceedings of the European Conference on Computer Vision*, pp. 754–770, 2020.

Wei-Ting Chen, Hao-Yu Fang, Cheng-Lin Hsieh, Cheng-Che Tsai, I Chen, Jian-Jiun Ding, Sy-Yen Kuo, et al. All snow removed: Single image desnowing algorithm using hierarchical dual-tree complex wavelet representation and contradict channel loss. In *Proceedings of the IEEE International Conference on Computer Vision*, pp. 4196–4205, 2021.

Xiang Chen, Hao Li, Mingqiang Li, and Jinshan Pan. Learning a sparse transformer network for effective image deraining. In *Proceedings of the IEEE/CVF conference on computer vision and pattern recognition*, 2023b.

Xiangyu Chen, Zheyuan Li, Yuandong Pu, Yihao Liu, Jiantao Zhou, Yu Qiao, and Chao Dong. A comparative study of image restoration networks for general backbone network design. In *European Conference on Computer Vision*, 2024.

Zheng Chen, Yulun Zhang, Jinjin Gu, Linghe Kong, Xiaokang Yang, and Fisher Yu. Dual aggregation transformer for image super-resolution. In *Proceedings of the IEEE/CVF international conference on computer vision*, pp. 12312–12321, 2023c.

Bodong Cheng, Juncheng Li, Ying Chen, Shuyi Zhang, and Tieyong Zeng. Snow mask guided adaptive residual network for image snow removal. *arXiv preprint arXiv:2207.04754*, 2022.

Sung-Jin Cho, Seo-Won Ji, Jun-Pyo Hong, Seung-Won Jung, and Sung-Jea Ko. Rethinking coarse-to-fine approach in single image deblurring. In *Proceedings of the IEEE International Conference on Computer Vision*, pp. 4641–4650, 2021.

Yuning Cui, Wenqi Ren, Xiaochun Cao, and Alois Knoll. Focal network for image restoration. In *Proceedings of the IEEE International Conference on Computer Vision*, pp. 13001–13011, 2023a.

Yuning Cui, Wenqi Ren, Xiaochun Cao, and Alois Knoll. Image restoration via frequency selection. *IEEE Transactions on Pattern Analysis and Machine Intelligence*, 2023b.

Yuning Cui, Wenqi Ren, Sining Yang, Xiaochun Cao, and Alois Knoll. Irnext: Rethinking convolutional network design for image restoration. In *Proceedings of the International Conference on Machine Learning*, 2023c.

Yuning Cui, Wenqi Ren, Xiaochun Cao, and Alois Knoll. Revitalizing convolutional network for image restoration. *IEEE Transactions on Pattern Analysis and Machine Intelligence*, 2024a.

Yuning Cui, Wenqi Ren, and Alois Knoll. Omni-kernel network for image restoration. In *Proceedings of the AAAI Conference on Artificial Intelligence*, volume 38, pp. 1426–1434, 2024b.

Yuning Cui, Syed Waqas Zamir, Salman Khan, Alois Knoll, Mubarak Shah, and Fahad Shahbaz Khan. Adair: Adaptive all-in-one image restoration via frequency mining and modulation. *arXiv preprint arXiv:2403.14614*, 2024c.

Hang Dong, Jinshan Pan, Lei Xiang, Zhe Hu, Xinyi Zhang, Fei Wang, and Ming-Hsuan Yang. Multi-scale boosted dehazing network with dense feature fusion. In *Proceedings of the IEEE Conference on Computer Vision and Pattern Recognition*, 2020a.

Yu Dong, Yihao Liu, He Zhang, Shifeng Chen, and Yu Qiao. Fd-gan: Generative adversarial networks with fusion-discriminator for single image dehazing. In *Proceedings of the AAAI Conference on Artificial Intelligence*, 2020b.

Deniz Engin, Anil Genc, and Hazim Kemal Ekenel. Cycle-dehaze: Enhanced cyclegan for single image dehazing. In *Proceedings of the IEEE Conference on Computer Vision and Pattern Recognition Workshops*, 2018.

Qingnan Fan, Dongdong Chen, Lu Yuan, Gang Hua, Nenghai Yu, and Baoquan Chen. A general decoupled learning framework for parameterized image operators. *IEEE Transactions on Pattern Analysis and Machine Intelligence*, 2019.

Zhenxuan Fang, Fangfang Wu, Weisheng Dong, Xin Li, Jinjian Wu, and Guangming Shi. Self-supervised non-uniform kernel estimation with flow-based motion prior for blind image deblurring. In *Proceedings of the IEEE/CVF conference on computer vision and pattern recognition*, pp. 18105–18114, 2023.

Xueyang Fu, Jie Xiao, Yurui Zhu, Aiping Liu, Feng Wu, and Zheng-Jun Zha. Continual image deraining with hypergraph convolutional networks. *IEEE Transactions on Pattern Analysis and Machine Intelligence*, 45(8):9534–9551, 2023.

Hongyun Gao, Xin Tao, Xiaoyong Shen, and Jiaya Jia. Dynamic scene deblurring with parameter selective sharing and nested skip connections. In *Proceedings of the IEEE Conference on Computer Vision and Pattern Recognition*, 2019.

Xin Gao, Tianheng Qiu, Xinyu Zhang, Hanlin Bai, Kang Liu, Xuan Huang, Hu Wei, Guoying Zhang, and Huaping Liu. Efficient multi-scale network with learnable discrete wavelet transform for blind motion deblurring. In *Proceedings of the IEEE/CVF Conference on Computer Vision and Pattern Recognition*, pp. 2733–2742, 2024.

Chun-Le Guo, Qixin Yan, Saeed Anwar, Runmin Cong, Wenqi Ren, and Chongyi Li. Image dehazing transformer with transmission-aware 3d position embedding. In *Proceedings of the IEEE Conference on Computer Vision and Pattern Recognition*, pp. 5812–5820, 2022.

Meng-Hao Guo, Cheng-Ze Lu, Zheng-Ning Liu, Ming-Ming Cheng, and Shi-Min Hu. Visual attention network. *Computational Visual Media*, 9(4):733–752, 2023a.

Yun Guo, Xueyao Xiao, Yi Chang, Shumin Deng, and Luxin Yan. From sky to the ground: A large-scale benchmark and simple baseline towards real rain removal. In *Proceedings of the IEEE/CVF International Conference on Computer Vision*, 2023b.

Kaiming He, Jian Sun, and Xiaoou Tang. Single image haze removal using dark channel prior. *IEEE Transactions on Pattern Analysis and Machine Intelligence*, 33(12):2341–2353, 2010.

Qibin Hou, Cheng-Ze Lu, Ming-Ming Cheng, and Jiashi Feng. Conv2former: A simple transformer-style convnet for visual recognition. *IEEE Transactions on Pattern Analysis and Machine Intelligence*, 2024.

Kui Jiang, Zhongyuan Wang, Peng Yi, Chen Chen, Baojin Huang, Yimin Luo, Jiayi Ma, and Junjun Jiang. Multi-scale progressive fusion network for single image deraining. In *Proceedings of the IEEE Conference on Computer Vision and Pattern Recognition*, 2020.

Yeying Jin, Beibei Lin, Wending Yan, Yuan Yuan, Wei Ye, and Robby T Tan. Enhancing visibility in nighttime haze images using guided apsf and gradient adaptive convolution. In *Proceedings of the ACM International Conference on Multimedia*, pp. 2446–2457, 2023.

Lingshun Kong, Jiangxin Dong, Jianjun Ge, Mingqiang Li, and Jinshan Pan. Efficient frequency domain-based transformers for high-quality image deblurring. In *Proceedings of the IEEE/CVF Conference on Computer Vision and Pattern Recognition*, pp. 5886–5895, 2023.

Junyong Lee, Hyeongseok Son, Jaesung Rim, Sunghyun Cho, and Seungyong Lee. Iterative filter adaptive network for single image defocus deblurring. In *Proceedings of the IEEE Conference on Computer Vision and Pattern Recognition*, pp. 2034–2042, 2021.

Boyi Li, Wenqi Ren, Dengpan Fu, Dacheng Tao, Dan Feng, Wenjun Zeng, and Zhangyang Wang. Benchmarking single-image dehazing and beyond. *IEEE Transactions on Image Processing*, 28 (1):492–505, 2018.

Boyun Li, Xiao Liu, Peng Hu, Zhongqin Wu, Jiancheng Lv, and Xi Peng. All-in-one image restoration for unknown corruption. In *Proceedings of the IEEE Conference on Computer Vision and Pattern Recognition*, 2022.

Yawei Li, Yuchen Fan, Xiaoyu Xiang, Denis Demandolx, Rakesh Ranjan, Radu Timofte, and Luc Van Gool. Efficient and explicit modelling of image hierarchies for image restoration. In *Proceedings of the IEEE/CVF Conference on Computer Vision and Pattern Recognition (CVPR)*, pp. 18278–18289, June 2023.

Jingyun Liang, Jiezhang Cao, Guolei Sun, Kai Zhang, Luc Van Gool, and Radu Timofte. Swinir: Image restoration using swin transformer. In *Proceedings of the IEEE International Conference on Computer Vision*, pp. 1833–1844, 2021.

Di Lin, Xin Wang, Jia Shen, Renjie Zhang, Ruonan Liu, Miaohui Wang, Wuyuan Xie, Qing Guo, and Ping Li. Generative status estimation and information decoupling for image rain removal. *Advances in Neural Information Processing Systems*, 35:4612–4625, 2022.

Chengxu Liu, Xuan Wang, Xiangyu Xu, Ruhao Tian, Shuai Li, Xueming Qian, and Ming-Hsuan Yang. Motion-adaptive separable collaborative filters for blind motion deblurring. In *Proceedings of the IEEE/CVF Conference on Computer Vision and Pattern Recognition*, pp. 25595–25605, 2024.

Keng-Hao Liu, Chia-Hung Yeh, Juh-Wei Chung, and Chuan-Yu Chang. A motion deblur method based on multi-scale high frequency residual image learning. *IEEE Access*, 8:66025–66036, 2020.

Lin Liu, Lingxi Xie, Xiaopeng Zhang, Shanxin Yuan, Xiangyu Chen, Wengang Zhou, Houqiang Li, and Qi Tian. Tape: Task-agnostic prior embedding for image restoration. In *European Conference on Computer Vision*, 2022.

Risheng Liu, Long Ma, Jiaao Zhang, Xin Fan, and Zhongxuan Luo. Retinex-inspired unrolling with cooperative prior architecture search for low-light image enhancement. In *Proceedings of the IEEE Conference on Computer Vision and Pattern Recognition*, 2021a.

Ye Liu, Lei Zhu, Shunda Pei, Huazhu Fu, Jing Qin, Qing Zhang, Liang Wan, and Wei Feng. From synthetic to real: Image dehazing collaborating with unlabeled real data. In *Proceedings of the ACM International Conference on Multimedia*, pp. 50–58, 2021b.

Ye Liu, Lei Zhu, Shunda Pei, Huazhu Fu, Jing Qin, Qing Zhang, Liang Wan, and Wei Feng. From synthetic to real: Image dehazing collaborating with unlabeled real data. In *Proceedings of the 29th ACM international conference on multimedia*, pp. 50–58, 2021c.

Yun-Fu Liu, Da-Wei Jaw, Shih-Chia Huang, and Jenq-Neng Hwang. Desnownet: Context-aware deep network for snow removal. *IEEE Transactions on Image Processing*, 27(6):3064–3073, 2018.

Xu Ma, Xiyang Dai, Yue Bai, Yizhou Wang, and Yun Fu. Rewrite the stars. In *Proceedings of the IEEE/CVF Conference on Computer Vision and Pattern Recognition*, pp. 5694–5703, 2024a.

Xu Ma, Xiyang Dai, Jianwei Yang, Bin Xiao, Yinpeng Chen, Yun Fu, and Lu Yuan. Efficient modulation for vision networks. In *The Twelfth International Conference on Learning Representations*, 2024b.

Xintian Mao, Jiansheng Wang, Xingran Xie, Qingli Li, and Yan Wang. Loformer: Local frequency transformer for image deblurring. In *ACM Multimedia 2024*, 2024.

David Martin, Charless Fowlkes, Doron Tal, and Jitendra Malik. A database of human segmented natural images and its application to evaluating segmentation algorithms and measuring ecological statistics. In *Proceedings of the IEEE International Conference on Computer Vision*, 2001.

Seungjun Nah, Tae Hyun Kim, and Kyoung Mu Lee. Deep multi-scale convolutional neural network for dynamic scene deblurring. In *Proceedings of the IEEE Conference on Computer Vision and Pattern Recognition*, 2017.

Vaishnav Potlapalli, Syed Waqas Zamir, Salman H Khan, and Fahad Shahbaz Khan. Promptir: Prompting for all-in-one image restoration. *Advances in Neural Information Processing Systems*, 2023.

Rui Qian, Robby T Tan, Wenhan Yang, Jiajun Su, and Jiaying Liu. Attentive generative adversarial network for raindrop removal from a single image. In *Proceedings of the IEEE conference on computer vision and pattern recognition*, pp. 2482–2491, 2018.

Xu Qin, Zhilin Wang, Yuanchao Bai, Xiaodong Xie, and Huizhu Jia. Ffa-net: Feature fusion attention network for single image dehazing. In *Proceedings of the AAAI Conference on Artificial Intelligence*, pp. 11908–11915, 2020.

Yuhui Quan, Shijie Deng, Yixin Chen, and Hui Ji. Deep learning for seeing through window with raindrops. In *Proceedings of the IEEE/CVF International Conference on Computer Vision*, pp. 2463–2471, 2019.

Lingyan Ruan, Bin Chen, Jizhou Li, and Miuling Lam. Learning to deblur using light field generated and real defocus images. In *Proceedings of the IEEE Conference on Computer Vision and Pattern Recognition*, pp. 16304–16313, 2022.

Noam Shazeer. Glu variants improve transformer. *arXiv preprint arXiv:2002.05202*, 2020.

Ziyi Shen, Wenguan Wang, Xiankai Lu, Jianbing Shen, Haibin Ling, Tingfa Xu, and Ling Shao. Human-aware motion deblurring. In *Proceedings of the IEEE International Conference on Computer Vision*, 2019.

Hyeongseok Son, Junyong Lee, Sunghyun Cho, and Seungyong Lee. Single image defocus deblurring using kernel-sharing parallel atrous convolutions. In *Proceedings of the IEEE International Conference on Computer Vision*, pp. 2642–2650, 2021.

Yuda Song, Zhuqing He, Hui Qian, and Xin Du. Vision transformers for single image dehazing. *arXiv preprint arXiv:2204.03883*, 2022.

Chunwei Tian, Yong Xu, and Wangmeng Zuo. Image denoising using deep cnn with batch renormalization. *Neural Networks*, 2020.

Fu-Jen Tsai, Yan-Tsung Peng, Yen-Yu Lin, Chung-Chi Tsai, and Chia-Wen Lin. Stripformer: Strip transformer for fast image deblurring. In *Proceedings of the European Conference on Computer Vision*, 2022.

Zhengzhong Tu, Hossein Talebi, Han Zhang, Feng Yang, Peyman Milanfar, Alan Bovik, and Yinxiao Li. Maxim: Multi-axis mlp for image processing. In *Proceedings of the IEEE Conference on Computer Vision and Pattern Recognition*, pp. 5769–5780, 2022.

Jeya Maria Jose Valanarasu, Rajeev Yasarla, and Vishal M. Patel. Transweather: Transformer-based restoration of images degraded by adverse weather conditions. In *Proceedings of the IEEE Conference on Computer Vision and Pattern Recognition*, pp. 2353–2363, 2022.

Tianyu Wang, Xin Yang, Ke Xu, Shaozhe Chen, Qiang Zhang, and Rynson W.H. Lau. Spatial attentive single-image deraining with a high quality real rain dataset. In *Proceedings of the IEEE/CVF Conference on Computer Vision and Pattern Recognition (CVPR)*, June 2019.

Zhendong Wang, Xiaodong Cun, Jianmin Bao, Wengang Zhou, Jianzhuang Liu, and Houqiang Li. Uformer: A general u-shaped transformer for image restoration. In *Proceedings of the IEEE Conference on Computer Vision and Pattern Recognition*, pp. 17683–17693, 2022.

Chen Wei, Wenjing Wang, Wenhan Yang, and Jiaying Liu. Deep retinex decomposition for low-light enhancement. *arXiv preprint arXiv:1808.04560*, 2018.

James CR Whittington, Timothy H Muller, Shirley Mark, Guifen Chen, Caswell Barry, Neil Burgess, and Timothy EJ Behrens. The tolman-eichenbaum machine: unifying space and relational memory through generalization in the hippocampal formation. *Cell*, 183(5):1249–1263, 2020.

James CR Whittington, Joseph Warren, and Timothy EJ Behrens. Relating transformers to models and neural representations of the hippocampal formation. *arXiv preprint arXiv:2112.04035*, 2021.

Jie Xiao, Xueyang Fu, Aiping Liu, Feng Wu, and Zheng-Jun Zha. Image de-raining transformer. *IEEE Transactions on Pattern Analysis and Machine Intelligence*, 2022.

Ke Xu, Xin Yang, Baocai Yin, and Rynson W.H. Lau. Learning to restore low-light images via decomposition-and-enhancement. In *Proceedings of the IEEE Conference on Computer Vision and Pattern Recognition*, 2020.

Xiaogang Xu, Ruixing Wang, Chi-Wing Fu, and Jiaya Jia. Snr-aware low-light image enhancement. In *Proceedings of the IEEE conference on computer vision and pattern recognition*, 2022.

Wending Yan, Robby T Tan, and Dengxin Dai. Nighttime defogging using high-low frequency decomposition and grayscale-color networks. In *Proceedings of the European Conference on Computer Vision*, pp. 473–488, 2020.

Jianwei Yang, Chunyuan Li, Xiyang Dai, and Jianfeng Gao. Focal modulation networks. *Advances in Neural Information Processing Systems*, 35:4203–4217, 2022.

Wenhan Yang, Robby T. Tan, Jiashi Feng, Jiaying Liu, Zongming Guo, and Shuicheng Yan. Deep joint rain detection and removal from a single image. In *Proceedings of the IEEE Conference on Computer Vision and Pattern Recognition*, 2017.

Wenhan Yang, Shiqi Wang, Yuming Fang, Yue Wang, and Jiaying Liu. Band representation-based semi-supervised low-light image enhancement: Bridging the gap between signal fidelity and perceptual quality. *IEEE Transactions on Image Processing*, 2021a.

Wenhan Yang, Wenjing Wang, Haofeng Huang, Shiqi Wang, and Jiaying Liu. Sparse gradient regularized deep retinex network for robust low-light image enhancement. *IEEE Transactions on Image Processing*, 2021b.

Tian Ye, Yunchen Zhang, Mingchao Jiang, Liang Chen, Yun Liu, Sixiang Chen, and Erkang Chen. Perceiving and modeling density for image dehazing. In *Proceedings of the European Conference on Computer Vision*, pp. 130–145, 2022.

Tian Ye, Sixiang Chen, Jinbin Bai, Jun Shi, Chenghao Xue, Jingxia Jiang, Junjie Yin, Erkang Chen, and Yun Liu. Adverse weather removal with codebook priors. In *Proceedings of the IEEE/CVF International Conference on Computer Vision*, pp. 12653–12664, 2023.

Weihao Yu and Xinchao Wang. Mambaout: Do we really need mamba for vision? *arXiv preprint arXiv:2405.07992*, 2024.

Syed Waqas Zamir, Aditya Arora, Salman Khan, Munawar Hayat, Fahad Shahbaz Khan, Ming-Hsuan Yang, and Ling Shao. Multi-stage progressive image restoration. In *Proceedings of the IEEE Conference on Computer Vision and Pattern Recognition*, pp. 14821–14831, 2021.

Syed Waqas Zamir, Aditya Arora, Salman Khan, Munawar Hayat, Fahad Shahbaz Khan, and Ming-Hsuan Yang. Restormer: Efficient transformer for high-resolution image restoration. In *Proceedings of the IEEE Conference on Computer Vision and Pattern Recognition*, pp. 5728–5739, 2022a.

Syed Waqas Zamir, Aditya Arora, Salman Khan, Munawar Hayat, Fahad Shahbaz Khan, Ming-Hsuan Yang, and Ling Shao. Learning enriched features for fast image restoration and enhancement. *IEEE Transactions on Pattern Analysis and Machine Intelligence*, 2022b.

Hongguang Zhang, Yuchao Dai, Hongdong Li, and Piotr Koniusz. Deep stacked hierarchical multi-patch network for image deblurring. In *Proceedings of the IEEE Conference on Computer Vision and Pattern Recognition*, 2019a.

Jiale Zhang, Yulun Zhang, Jinjin Gu, Jiahua Dong, Linghe Kong, and Xiaokang Yang. Xformer: Hybrid x-shaped transformer for image denoising. In *The Twelfth International Conference on Learning Representations*, 2024.

Jing Zhang, Yang Cao, Shuai Fang, Yu Kang, and Chang Wen Chen. Fast haze removal for nighttime image using maximum reflectance prior. In *Proceedings of the IEEE Conference on Computer Vision and Pattern Recognition*, 2017.

Jinghao Zhang, Jie Huang, Mingde Yao, Zizheng Yang, Hu Yu, Man Zhou, and Feng Zhao. Ingredient-oriented multi-degradation learning for image restoration. In *Proceedings of the IEEE Conference on Computer Vision and Pattern Recognition*, 2023.

Kaihao Zhang, Wenhan Luo, Yiran Zhong, Lin Ma, Bjorn Stenger, Wei Liu, and Hongdong Li. Deblurring by realistic blurring. In *Proceedings of the IEEE Conference on Computer Vision and Pattern Recognition*, 2020.

Yonghua Zhang, Jiawan Zhang, and Xiaojie Guo. Kindling the darkness: A practical low-light image enhancer. In *Proceedings of the 27th ACM international conference on multimedia*, 2019b.

Shihao Zhou, Duosheng Chen, Jinshan Pan, Jinglei Shi, and Jufeng Yang. Adapt or perish: Adaptive sparse transformer with attentive feature refinement for image restoration. In *Proceedings of the IEEE/CVF conference on computer vision and pattern recognition*, 2024a.

Shihao Zhou, Jinshan Pan, Jinglei Shi, Duosheng Chen, Lishen Qu, and Jufeng Yang. Seeing the unseen: A frequency prompt guided transformer for image restoration. In *European Conference on Computer Vision*, 2024b.

APPENDIX

This appendix provides more experimental results, ablation studies, and visual comparisons.

A MORE EXPERIMENTAL RESULTS

In this section, we first provide experimental results on LOL-V2 (Yang et al., 2021b) for low-light image enhancement. The numerical results are presented in Table 11. Our method significantly outperforms the Transformer-based algorithm Retinexformer (Cai et al., 2023) by 0.43 dB PSNR. The visual results are illustrated in Figure 10. Our model recovers more edges from the input image. These results suggest the strong potential of our method for low-light image enhancement.

Table 11: Numerical comparisons on the LOL-V2-synthetic dataset (Yang et al., 2021b) for low-light image enhancement.

Methods	PSNR	SSIM
RUAS (Liu et al., 2021a)	16.55	0.652
FIDE (Xu et al., 2020)	15.20	0.612
DRBN (Yang et al., 2021a)	23.22	0.927
KinD (Zhang et al., 2019b)	13.29	0.578
Restormer (Zamir et al., 2022a)	21.41	0.830
MIRNet (Zamir et al., 2022b)	21.94	0.876
SNR-Net (Xu et al., 2022)	24.14	0.928
Retinexformer (Cai et al., 2023)	25.67	0.930
Ours	**26.10**	**0.944**

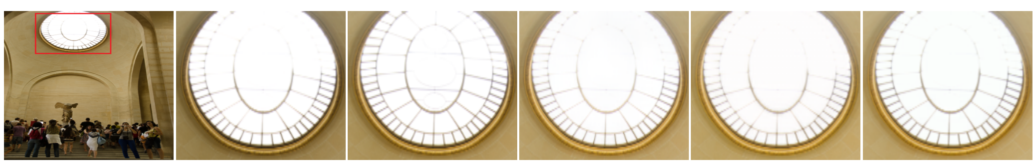

Input Reference SNR Retinexformer Ours

Figure 10: Visual results on LOL-V2-Synthetic (Yang et al., 2021b).

Table 12: The numerical comparisons on five image restoration tasks under the all-in-one setting: dehazing (SOTS (Li et al., 2018)), deraining (Rain100L (Yang et al., 2017)), denoising (BSD68 (Martin et al., 2001)), deblurring (GoPro (Nah et al., 2017)), and low-light image enhancement (LOL-V1 (Wei et al., 2018)). The results are reported in the form of PSNR/SSIM.

Method	Dehazing	Deraining	Denoising	Deblurring	Low-Light	Average
NAFNet (Chen et al., 2022)	25.23/0.939	35.56/0.967	31.02/0.883	26.53/0.808	20.49/0.809	27.76/0.881
MPRNet (Zamir et al., 2021)	24.27/0.937	**38.16**/0.981	31.35/0.889	26.87/0.823	20.84/0.824	28.27/0.890
MIRNetV2 (Zamir et al., 2022b)	24.03/0.927	33.89/0.954	30.97/0.881	26.30/0.799	21.52/0.815	27.34/0.875
SwinIR (Liang et al., 2021)	21.50/0.891	30.78/0.923	30.59/0.868	24.52/0.773	17.81/0.723	25.04/0.835
Restormer (Zamir et al., 2022a)	24.09/0.927	34.81/0.962	31.49/0.884	27.22/0.829	20.41/0.806	27.60/0.881
DL (Fan et al., 2019)	20.54/0.826	21.96/0.762	23.09/0.745	19.86/0.672	19.83/0.712	21.05/0.743
Transweather (Valanarasu et al., 2022)	21.32/0.885	29.43/0.905	29.00/0.841	25.12/0.757	21.21/0.792	25.22/0.836
TAPE (Liu et al., 2022)	22.16/0.861	29.67/0.904	30.18/0.855	24.47/0.763	18.97/0.621	25.09/0.801
AirNet (Li et al., 2022)	21.04/0.884	32.98/0.951	30.91/0.882	24.35/0.781	18.18/0.735	25.49/0.846
IDR (Zhang et al., 2023)	25.24/0.943	35.63/0.965	**31.60**/0.887	27.87/0.846	21.34/0.826	28.34/0.893
Ours	**30.29/0.978**	38.08/**0.982**	31.37/**0.891**	**28.31/0.860**	**22.89/0.855**	**30.19/0.913**

Moreover, we report experimental results under all-in-one image restoration, *i.e.,* five-task setting. The quantitative results are presented in Table 12. As seen, our method achieves a PSNR score of

30.19 when averaging across all tasks, which is 1.85 dB higher than that of IDR (Zhang et al., 2023). In particular, for the dehazing problem, our model significantly outperforms the second-best algorithm (Zhang et al., 2023) by 5.05 dB PSNR. Despite not incorporating a complex dynamic mechanism for identifying degradation types, aside from SA, our method consistently delivers promising results across various all-in-one tasks, thanks to its robust representational capability.

Table 13: Ablation studies of the deployment strategy for different kinds of attention.

Scale 0	Scale 1	Scale 2	PSNR
Spatial	Spatial	Spatial	31.76
Channel	Spatial	Spatial	31.82
Channel	Channel	Spatial	31.62
Channel	Channel	Channel	31.55
Normal Attention (Zamir et al., 2022a)			31.50

Table 14: More ablation studies for DFFN.

Methods	PSNR
Ours	31.82
only frequency branch in spatial-spectral interactions	31.76
w/o attention weight for spatial-spectral fusion	31.73

B More ablation studies

Deployment strategy for attention. We apply channel-wise modulation block in the first scale while using spatial-wise block in other scales, as spatial-wise SA is more expensive than channel version when modeling large-scale features. In our case, the first scale includes the highest-resolution features. Table 13 shows that our strategy achieves the best performance. Moreover, we experiment by using only regular channel attention Zamir et al. (2022a) in all scales, achieving a 0.32 dB lower performance than our full model. These results validate the efficacy of our design.

DFFN. We conduct more ablation studies for DFFN by removing or substituting certain operators. Table 14 shows that removing the spatial branch in inter-domain fusion achieves 31.76 dB PSNR, suggesting the significance of dual-domain feature fusion. Removing the attention weights leads to 31.73 dB PSNR, which is even lower than the result of using a single branch, *e.g.,* frequency branch (31.76 dB), demonstrating the importance of coordinating the fusion process.

Modulation design. In this part, we perform ablation studies for the modulation design. We use the plain depth-wise convolutions with the same kernel size to supplant the filter operation, achieving 31.69 dB PSNR, which is 0.13 dB lower than our design.

Parameter-sharing mechanism. In our model, we share the parameters across CMB. We carry out experiments to apply the parameter-sharing strategy in deeper scales, achieving lower performance than our design (see Table 15). We also attempt to further share the parameters among DFFN in the first scale, obtaining only 30.53 dB PSNR. Therefore, we only apply the mechanism in CMB for better performance.

Position of downsampling. In CMB, we apply downsampling after the convolutions, which can fully learn the spatial connectivity, as the channel-wise SA layer cannot model the real spatial pixel interactions. We experiment by moving downsampling before convolutions, saving 1.89 GFLOPs while achieving 0.11 dB lower PSNR. Finally, we choose to place downsampling after convolutions in the CMB of our model.

Table 15: Abltion studies for the parameter-sharing mechanism. Scale 0,1,2 means sharing parameters within each scale of all scales.

Method	PSNR
Scale 0	31.82
Scale 0,1	31.82
Scale 0,1,2	31.82

C MORE VISUAL RESULTS

Visual comparisons on more datasets are illustrated in Figure 11 and Figure 12.

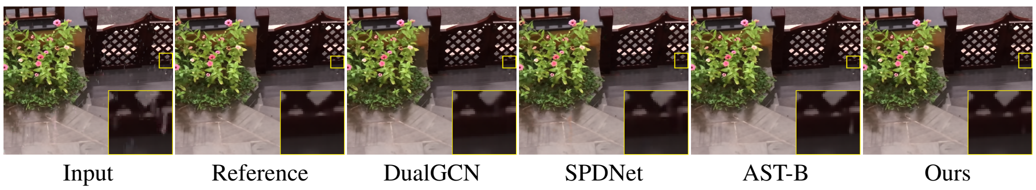

Figure 11: Image deraining comparisons on the SPAD (Wang et al., 2019) dataset.

Figure 12: Motion deblurring comparisons on the HIDE (Shen et al., 2019) dataset.